Simulation of an optomechanical quantum memory in the nonlinear regime

R. Y. Teh, S. Kiesewetter, M. D. Reid, and P. D. Drummond

Centre for Quantum and Optical Science, Swinburne University of Technology, Melbourne, Australia

Optomechanical systems cooled to the quantum level provide a promising mechanism for a high-fidelity quantum memory that is faithful to a given temporal mode structure, and can be recovered synchronously. We carry out full, probabilistic quantum simulation of a quantum optomechanical memory, including nonlinear effects that are usually ignored. This is achieved using both the approximate truncated Wigner and the exact positive P phase-space representations. By considering the nonlinear quantum optomechanical Hamiltonian, our simulations allow us to probe the regime where the linearization approximation fails to hold. We show evidence for large spectral overlap between the quantum signal and the transfer field in typical optomechanical quantum memory experiments. Methods for eliminating this overlap to accurately recover the quantum signal are discussed. This allows us to give a complete model for the quantum storage of a coherent state. We treat the mode matching that is necessary to accurately retrieve the stored quantum state, by including the internal dynamics of the mechanical system as well as the optical system. We also include the finite switching time of the control transfer field. The fidelity for the storage of a coherent state is computed numerically using currently realistic experimental parameters in the electromechanical case. We find the expected fidelity is lower than required to demonstrate true quantum state transfers. Significant improvements in the quality factor of the cavity and mechanical systems will, however, increase the fidelity beyond the quantum threshold.

I. INTRODUCTION

A quantum memory is a device that stores quantum states. Optomechanics is a good candidate for a quantum memory: there are standard quantum optical techniques for the generation of quantum states of light that can be shaped temporally and spatially. These quantum states can be stored in long-lived mechanical modes via a radiation pressure interaction. A quantum memory has important applications in proposed quantum internet systems [1–3], where a network of nodes is connected by optical fibers. There are many other proposed applications as well. Generally, optomechanical nodes can transmit and receive optical quantum states, which can be stored in mechanical oscillators at each node with low dissipation. Advances in mechanical quantum ground-state cooling techniques [4–7] further reduce the spurious effects of thermal noise entering the optomechanical system.

Most experiments and theoretical analyses to date are based on a linearized optomechanical Hamiltonian [8–10], the adiabatic approximation [8,11], or both. The linearized optomechanical interaction is sufficient to describe optomechanical ground-state cooling [4–6], state transfer [11,12], and Einstein-Podolsky-Rosen entanglement generation [8–10,13–15]. However, a nonlinear quantum interaction is needed for the creation of highly nonclassical states for the mechanical mode such as Fock states and Schrödinger's cat states [16], and generically all optomechanical systems have nonlinearities. We will show that such nonlinearities have very significant effects on spectral intensities in experiments, even in weak-coupling regimes where these approximations are often used.

In this paper, we consider the nonlinear Hamiltonian describing the radiation pressure interaction in optomechanical systems. In particular, we analyze a two-pulse quantum state transfer protocol using phase-space simulations in both the approximate truncated Wigner [17,18] and exact positive P [19] representations. These phase-space methods, without the linearization approximation, allow us to study the quantum

optomechanical system in the nonlinear, strongly coupled quantum regime, where a single photon can affect the mechanical motion [16]. Our aim is to develop such a nonlinear model, but specifically to determine the implication of nonlinearity for quantum memory in regimes corresponding to current experimental parameters.

One of our main results concerns the spectral overlap between pump and signal fields. A detuned pump field enhances the optomechanical coupling strength and facilitates quantum state transfer between the optical and mechanical modes. In a linearized theory, the optical mode amplitude is separated into two components: a large steady-state amplitude induced by the pump field and a smaller time-dependent "signal" amplitude due to the quantum state. It is assumed that the two different amplitudes are distinguishable. In particular, they should be well separated in the frequency space.

Our nonlinear analysis indicates this is typically not the case in current experiments. Using published experimental parameters for phase-space simulations, we observe large spectral content overlaps, in agreement with experimental observations [20]. We address this issue by discussing methods for eliminating this problem. We also obtain analytical results using the linearized scheme, and compare them with nonlinear phase-space simulation results. Our conclusion is that nonlinearity due to the intense pump field has to be taken into account. This is especially so in the strong-coupling regime where the effective optomechanical coupling strength is larger than the optical cavity decay rate ($g > \gamma_o$).

An essential part of our analysis is to accurately treat mode matching [21]. Mode matching is used to retrieve the quantum state stored in the mechanics, where a temporal mode function, mode matched to the output field mode function, is mixed with the output field with a beam splitter. This approach retains both the amplitude and phase of the quantum state stored, in contrast to the more widely used approach where the power spectra are recorded. Power spectral information only contains the information of the intensity of quantum

states stored, while the phase information is lost. Thus, a mode matching approach is necessary for a quantum memory that stores quantum superpositions.

In our treatment, we also model the preparation and transfer control fields that create and transfer the quantum state between the cavity and the mechanical mode. The fidelity for the storage of a coherent state is then computed and compared with the benchmark fidelity criterion for a quantum memory [22]. We apply the nonlinear analysis to give a complete model of the electromechanical experiment of Ref. [12]. We are also able to include the effect of the finite switching time of the transfer field, which cannot easily be done in the linearized model. We point out that the optimal mode matching pulse shape for best fidelity is different than a simple exponential, owing to the effect of the internal dynamics of the optomechanical system.

To summarize, we find that there are substantial differences between the usual adiabatic linearized models and both of the calculations obtained here that use a full nonlinear simulation. This is mostly because assumed frequency separations within realistic parameter ranges are not sufficient to fully separate control and signal fields, as is often assumed analytically. The physics involved is simple enough: signal fields have to be relatively weak to be in the quantum regime, and can easily be comparable to the frequency tails of a control field. This requires more sophisticated techniques to separate the two. Generally speaking, the exact positive P and the approximate truncated Wigner methods give similar results for current experimental parameters, although nonlinear effects can be significant. This confirms that the truncated Wigner method is accurate with these parameter values, although the exact positive P method will be needed in highly nonlinear regimes.

The paper is organized as follows. Section II provides a brief description of a generic quantum optomechanical system. We consider a particular optomechanical state transfer protocol and discuss that in detail. In Sec. III, stochastic differential equations used to simulate the optomechanical state transfer are presented. We then present our simulation results in Sec. V and discuss some subtleties in an optomechanical state transfer experiment due to the spectral overlap issue.

II. OPTOMECHANICAL MODEL

We describe a two-pulse optomechanical state transfer protocol. In this paper, the state transfer protocol is used to study optomechanical quantum memory of a coherent state. However, this protocol can be applied to arbitrary quantum states such as Schrödinger's cat states. In this section, the fundamental model is described.

A. Quantum optomechanical Hamiltonian and master equation

A typical quantum optomechanical system consists of a Fabry-Perot cavity with one of the movable mirrors acting as a mechanical oscillator (Fig. 1). Interactions between the cavity and mechanical degrees of freedom are mediated through the radiation pressure where photons impart momentum on the mirror. External laser fields are coupled into the cavity in various quantum information protocols. It is convenient to transform into the rotating frame of the external laser field,
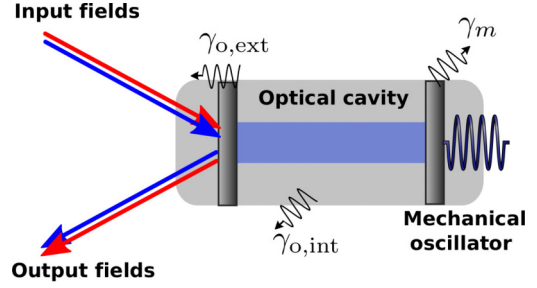

FIG. 1. A typical optomechanical system.

leading to the Hamiltonian [9]

$$
H = \hbar \Delta a^\dagger a + \hbar \omega_m b^\dagger b + \hbar g_0 a^\dagger a (b + b^\dagger)
$$
$$
- i\hbar \sqrt{2\gamma_{\text{ext}}} [\epsilon(t) a - \epsilon^*(t) a^\dagger], \tag{1}
$$

where a, b are the quantum annihilation operators for the cavity field and mechanical oscillator modes respectively, and $\Delta = \omega_c - \omega_d$ is the detuning between the cavity resonance frequency ω_c and the external laser carrier frequency ω_d. The first two terms correspond to the energy of the cavity and mechanical oscillator at ω_m, respectively. The third term describes the interaction between the cavity and mechanical oscillator due to radiation pressure and the last term describes the coherent input $\epsilon(t)$, where γ_{ext} is an external cavity decay rate which determines the strength of coupling of the cavity to the external input field.

In practice, the optomechanical system always interacts with its environment, resulting in decoherence through damping and fluctuations. We model these effects with the standard open system formalism using a density operator. Assuming interactions with the environment to be Markovian, the master equation for the open system is [23]

$$
\frac{d}{dt}\rho = -\frac{i}{\hbar}[H,\rho] + \sum_j \gamma_j \bar{n}_j (2a_j^\dagger \rho a_j - a_j \rho a_j^\dagger - \rho a_j a_j^\dagger)
$$
$$
+ \sum_j \gamma_j (\bar{n}_j + 1)(2a_j \rho a_j^\dagger - a_j^\dagger a_j \rho - \rho a_j^\dagger a_j). \tag{2}
$$

The index $j = 1, 2 \sim o,m$ refers to the cavity and mechanical modes, respectively, while γ_o and γ_m are the cavity decay rate and mechanical dissipation rate, respectively, and $\bar{n}_j$ are the average thermal occupation numbers from interactions with their corresponding reservoirs. The decay rates are for amplitudes.

We distinguish two contributions to the cavity decay rate that corresponds to different sources of losses, $\gamma_o = \gamma_{\text{ext}} + \gamma_{\text{int}}$. The *external* cavity decay rate γ_{ext} comes from the cavity field leaking out of the cavity—which determines the input coupling by reciprocity—while the *internal* cavity decay rate γ_{int} includes all other sources of dissipation in the cavity.

An equivalent set of quantum Langevin equations can be derived from the master equation in Eq. (2). They give the time evolution of the cavity and mechanical mode operators [23]. In general, neither the master equation nor the quantum Langevin equations can be solved analytically, and numerical solutions are required.

B. Optomechanical state transfer protocol

An optomechanical quantum memory requires quantum state transfers between the optical and mechanical system with
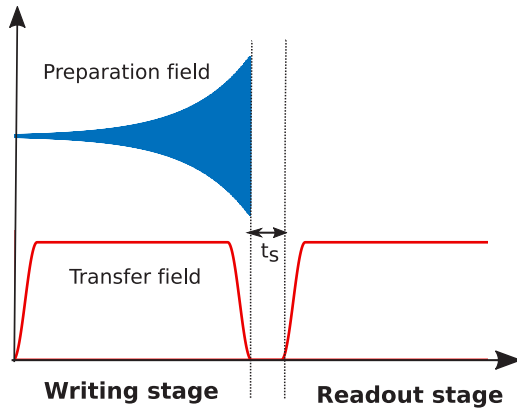
FIG. 2. The two-pulse optomechanical state transfer protocol, where t_s is the storage time of the quantum state in the mechanical mode.

minimal degradation and loss. The state transfer protocol in this paper is based on the fact that a red-detuned control field transfers quantum states between the cavity and mechanical oscillator. Analyses on how a detuned field transfers quantum states between the optical and mechanical modes can be found, for example, in the review by Meystre [24].

We consider a particular state transfer protocol as shown in Fig. 2, that involves two external field pulses, which we call the preparation and transfer fields [12]. The preparation or signal field generates the cavity quantum state that is to be stored in the quantum memory and the transfer or control field facilitates the quantum state transfer between the cavity and mechanical modes. The preparation field has the same frequency as the resonance frequency of the resonator ω_c while the transfer field has frequency ω_d such that the detuning Δ between the resonator and the transfer field frequency is the frequency of the mechanical oscillator, i.e., $\Delta = \omega_c - \omega_d = \omega_m$.

The optomechanical state transfer protocol consists of three stages. The writing stage involves sending the quantum state into the cavity and transferring it into the mechanical system. During this stage, both the preparation and transfer fields are applied. This simultaneously generates the cavity quantum state and transfers it to the mechanical mode. After the quantum state is completely transferred to the mechanical mode, both fields are turned off in the storing stage. Due to the low mechanical decay rate γ_m, the mechanical oscillator serves as a good quantum memory. The stored quantum state will retain its coherence on a time scale of $1/\gamma_m$. Finally, a second transfer field is applied in the readout stage. This transfers the quantum state from the mechanical mode back into the cavity, which will then leak out of the cavity and subsequently be detected.

Based on the Hamiltonian in Eq. (1), the optomechanical quantum memory Hamiltonian is expressed as

$$\tilde{H} = \hbar\omega_m a^\dagger a + \hbar\omega_m b^\dagger b + \hbar g_0 a^\dagger a(b + b^\dagger)$$
$$- i\hbar\sqrt{2\gamma_{\text{ext}}}[\epsilon(t)a - \epsilon^*(t)a^\dagger], \qquad (3)$$

where we choose a rotating frame with $\Delta = \omega_m$, and $\epsilon(t) = \epsilon_{\text{trans}}(t) + \epsilon_{\text{prep}}(t)e^{-i\omega_m t}$. Here, $\epsilon_{\text{trans}}(t)$ and $\epsilon_{\text{prep}}(t)$ correspond to the transfer field and preparation field amplitudes, respectively. We choose to transform into the rotating frame of the

transfer field, leaving the preparation field oscillating at the resonance frequency of the mechanical oscillator ω_m. We give more details of the precise time dependence of control and signal fields in later sections.

We note here that our simulations used an optimal mode-matched pulse shape, calculated using the linearized equations of motion [21]. We employed the same pulse shapes in all simulations, both linear and nonlinear, for consistency. Recent experiments [12] used a simplified version of this which, although similar, is not quite optimal.

III. PHASE-SPACE METHODS

Both the master equation and quantum Langevin equations described in Sec. II A are nonlinear operator equations. Approximate results can be obtained in the single mode optomechanical model using linearization [25]. However, analytical solutions without any approximations do not appear to exist. In addition to the nonlinear terms in the operator equations, the Hilbert space grows exponentially with the number of modes.

The effect of the large Hilbert space is that it makes these equations extremely complex if one uses a standard, orthogonal number-state basis. Instead, phase-space methods transform the master equation in Eq. (2) into a set of corresponding c-number stochastic differential equations. The techniques and algorithms required to solve these stochastic differential equations numerically are well established [26–29].

In this paper, we use the approximate truncated Wigner and exact positive P representations. Both the truncated Wigner [17,18] and positive P representations [19] have been employed in previous work on pulsed entanglement and Einstein-Podolsky-Rosen steering in optomechanics [15].

Phase-space representations

Using operator identities for both the truncated Wigner and positive P representations, we derive their corresponding Fokker-Planck equations and equivalent sets of stochastic differential equations, as follows.

1. Truncated Wigner representation

The Wigner representation provides a complete mapping of the density matrix for the quantum system into a quasiprobability $W(\alpha, \beta, \alpha_{\text{out}})$. This is used to represent the output modes as well as the internal modes of the system. We note that the input modes are treated as external finite temperature reservoirs, together with a coherent displacement term $\epsilon(t)$ in the Hamiltonian, which models the effect of an additional coherent driving field in the experiments.

The Wigner function W is not always a probability density, as it can develop negative values. It also does not have a positive-definite Fokker-Planck equation. Its equation of motion has third-order derivatives. However, if the third-order derivative terms are truncated, one can obtain an approximate, positive-definite time-evolution equation for W.

This equation is equivalent to an ensemble of stochastic differential equations, which can be readily simulated numerically. The resulting stochastic differential equations that dictate the time evolutions of the optical mode α and mechanical mode

β amplitudes are given, respectively, by

$$d\alpha = \{-[i\omega_m + ig_0(\beta + \beta^*) + \gamma_0]\alpha\}dt + d\alpha_{\text{in}},$$

$$d\beta = \{-[i\omega_m + \gamma_m]\beta - ig_0|\alpha|^2\}dt + d\beta_{\text{in}}, \quad (4)$$

where the input field terms are

$$d\alpha_{\text{in}} = \sqrt{2\gamma_{\text{ext}}}\epsilon(t)dt + \sqrt{2\gamma_{\text{ext}}}d\alpha_{\text{ext}}^{\text{in}} + \sqrt{2\gamma_{\text{int}}}d\alpha_{\text{int}}^{\text{in}}$$

$$\equiv \sqrt{2\gamma_{\text{ext}}}d\alpha_{\text{total}}^{\text{in}} + \sqrt{2\gamma_{\text{int}}}d\alpha_{\text{int}}^{\text{in}}, \quad (5)$$

$$d\beta_{\text{in}} = \sqrt{2\gamma_m}d\beta^{\text{in}}.$$

The external input field α_{in} consists of a coherent input $\epsilon(t)$, together with broadband quantum noise inputs associated with the external and internal cavity reservoirs. These have thermal Gaussian noises, with thermal occupation numbers $\bar{n}_i$ for the optical and acoustic reservoirs, which satisfy

$$\langle d\alpha_i^{\text{in}} d\alpha_j^{\text{in}*}\rangle = \left(\bar{n}_i + \tfrac{1}{2}\right)\delta_{ij}dt. \quad (6)$$

The input into the cavity and the output from the cavity are related by the well-known input-output relation [30]

$$\alpha_{\text{out}}(t) = \sqrt{2\gamma_{\text{ext}}}\alpha(t) - \alpha_{\text{total}}^{\text{in}}(t). \quad (7)$$

Here $\alpha_{\text{total}}^{\text{in}}(t)$ includes the coherent input field $\epsilon(t)$ and noises entering the cavity $\alpha_{\text{ext}}^{\text{in}}$, but not noises due to internal cavity losses. This formalism models a high-Q cavity, in which the external inputs are almost entirely reflected, together with some leakage at a rate γ_{ext} from the cavity to the external field.

The integrated input and output mode amplitudes are obtained by integrating these modes with their corresponding temporal mode functions $u_{\text{in}}(t)$ and $u_{\text{out}}(t)$ as given below:

$$A_{\text{in}} = \int_{-\infty}^{0} u_{\text{in}}^*(\tau)\alpha_{\text{total}}^{\text{in}}(\tau)\,d\tau,$$

$$A_{\text{out}} = \int_{t_s}^{\infty} u_{\text{out}}^*(\tau)\alpha_{\text{out}}(\tau)\,d\tau, \quad (8)$$

where t_s is storage time of the quantum state in the mechanical mode.

This classical-like equation is only approximate. As well as sampling errors from the use of stochastic equations, there is a truncation of third-order derivative terms in the Wigner dynamical equation, which are higher-order terms in an expansion in inverse boson number. This can sometimes lead to incorrect results [31], especially for weak fields [32] and third-order correlations [33]. In addition, the phase-space representation directly represents symmetrically ordered operators, while measurements are usually for normal ordering.

2. Positive P representation

The positive P representation does not require the approximation used in the truncated Wigner representation. Hence, it is exact apart from a controllable sampling error, provided boundary terms due to power-law distribution tails are negligible [34]. There are techniques available to remove these if necessary [35]. No evidence of large distribution tails or boundary terms was found in the work reported here.

This method always has a positive distribution for any quantum density matrix, but has twice the phase-space dimension, so it has six independent complex variables, $P(\alpha, \alpha^+, \beta, \beta^+, \alpha_{\text{out}}, \alpha_{\text{out}}^+)$. Since the number of independent

complex phase-space variables is increased due to this dimension doubling approach, the corresponding stochastic differential equations are, using standard differential identities [15,19,36]

$$d\alpha = \{-[i\omega_m + \gamma_0 + ig_0(\beta + \beta^+)]\alpha\}dt + d\alpha_{\text{in}},$$

$$d\beta = \{-[i\omega_m + \gamma_m]\beta - ig_0\alpha^+\alpha\}dt + d\beta_{\text{in}},$$

$$d\alpha^+ = \{[i\omega_m - \gamma_0 + ig_0(\beta + \beta^+)]\alpha^+\}dt + d\alpha_{\text{in}}^+,$$

$$d\beta^+ = \{[i\omega_m - \gamma_m]\beta^+ + ig_0\alpha^+\alpha\}dt + d\beta_{\text{in}}^+, \quad (9)$$

where

$$d\alpha_{\text{in}} = \sqrt{2\gamma_{\text{ext}}}\epsilon(t)dt + \sqrt{2\gamma_{\text{ext}}}d\alpha_{\text{ext}}^{\text{in}} + \sqrt{2\gamma_{\text{int}}}d\alpha_{\text{int}}^{\text{in}} + d\alpha_g,$$

$$d\beta_{\text{in}} = \sqrt{2\gamma_m}d\beta^{\text{in}} + d\beta_g,$$

$$d\alpha_{\text{in}}^+ = \sqrt{2\gamma_{\text{ext}}}\epsilon^*(t)dt + \sqrt{2\gamma_{\text{ext}}}d\alpha_{\text{ext}}^{\text{in}*} + \sqrt{2\gamma_{\text{int}}}d\alpha_{\text{int}}^{\text{in}*} + d\alpha_g^+,$$

$$d\beta_{\text{in}}^+ = \sqrt{2\gamma_m}d\beta^{\text{in}*} + d\beta_g^+. \quad (10)$$

In the positive P representation, there are independent noise terms due to the nonlinear interaction between the different modes. These are given by $d\alpha_g$, $d\alpha_g^+$, $d\beta_g$, and $d\beta_g^+$ and the only nonzero correlations between them are

$$\langle d\alpha_g d\beta_g\rangle = -ig_0\alpha dt,$$

$$\langle d\alpha_g^+ d\beta_g^+\rangle = ig_0\alpha^+ dt. \quad (11)$$

The thermal Gaussian noises are similar to those in the truncated Wigner representation, except that they correspond to normally ordered, not symmetrically ordered, fluctuations:

$$\langle d\alpha_i^{\text{in}} d\alpha_j^{\text{in}*}\rangle = \bar{n}_i\delta_{ij}dt. \quad (12)$$

The integrated input and output mode amplitudes are identical to those defined in Eq. (8). This approach gives a direct representation of normally ordered operators.

IV. LINEARIZED QUANTUM MEMORY MODEL

The cavity amplitude can be expressed in terms of a set of orthogonal temporal transverse modes. In this paper, we are concerned with the storage of the coherent cavity amplitude in one of these temporal modes. In order to optimize the coupling between the preparation field and the cavity, the preparation field containing the coherent state to be stored in the optomechanical system has to temporally mode match one of these orthogonal cavity temporal modes. Perfect mode matching ensures that only the intended cavity mode will remain in the cavity and other modes will either be reflected or leak out of the cavity.

The optimal mode function for the preparation field within the linearization approximation was first obtained by He *et al.* [21,37]. These linearized calculations are instructive as they provide a simple theoretical description of the subsequent experimental demonstrations of coherent-state transfer [12]. In this section, we include linearized calculations similar to those of He *et al.* [21], but taking into account internal cavity losses. In their work, He *et al.* solved the stochastic differential equations describing the time evolution of both the cavity $a(t)$ and mechanical modes $b(t)$. Those equations are derived from the effective interaction Hamiltonian

$$H_{\text{int}} = \hbar g(ab^\dagger + a^\dagger b), \quad (13)$$

where $g = g_0\sqrt{N}$ is the effective coupling and N is the intracavity photon number of the transfer field.

The interaction Hamiltonian in Eq. (13) requires the use of linearization and rotating wave approximations. These approximations are justified in many of the optomechanical experiments to date, due to the weak bare coupling strength g_0, and an intense pump field is required to enhance the optomechanical coupling strength. One of the objectives of this paper is to analyze whether these approximations are valid in optomechanical quantum memory experiments.

The corresponding linearized Heisenberg time evolution equations

$$\frac{d}{dt}a(t) = -\gamma_o a - igb + \sqrt{2\gamma_{\text{ext}}}a_{\text{ext}}^{\text{in}} + \sqrt{2\gamma_{\text{int}}}a_{\text{int}}^{\text{in}},$$

$$\frac{d}{dt}b(t) = -\gamma_m b - iga + \sqrt{2\gamma_m}b^{\text{in}} \quad (14)$$

can be solved analytically. The general solution $\vec{a}(t) = \binom{a(t)}{b(t)}$ for the writing stage is

$$\vec{a}(t) = \int_{-\infty}^{t} e^{\kappa_+ \tau}\cosh(m\tau)I\vec{a}_{\text{in}}(\tau)\,d\tau$$

$$+ \int_{-\infty}^{t} e^{\kappa_+ \tau}\frac{\sinh(m\tau)}{m}\begin{pmatrix} \kappa_- & ig \\ ig & -\kappa_- \end{pmatrix}\vec{a}_{\text{in}}(\tau)\,d\tau, \quad (15)$$

where $\quad \vec{a}_{\text{in}}(t) = \binom{\sqrt{2\gamma_{\text{ext}}}a_{\text{ext}}^{\text{in}} + \sqrt{2\gamma_{\text{int}}}a_{\text{int}}^{\text{in}}}{\sqrt{2\gamma_m}b^{\text{in}}}$, $\quad \kappa_+ = (\gamma_o + \gamma_m)/2$, $\kappa_- = (\gamma_o - \gamma_m)/2$, and $m = \sqrt{\kappa_-^2 - g^2}$. The preparation field in the optomechanical state transfer protocol is $a_{\text{ext}}^{\text{in}} = a_0 u_{\text{in}}$, where a_0 is the initial mode-matched external field operator the coherent amplitude of which we want to store, and u_{in} is the temporal external mode function yet to be determined.

In particular, the stored mode in the mechanical system is given by

$$b(0) = \sqrt{2\gamma_{\text{ext}}}\int_{-\infty}^{0}\frac{ig}{m}a_0 u_{\text{in}}(\tau)e^{\kappa_+ \tau}\sinh(m\tau)\,d\tau + \text{noise}. \quad (16)$$

From the mechanical mode amplitude solution above, it can be shown that the optimal mode function is of the form

$$u_{\text{in}}(t) = -2i\frac{\sqrt{(\kappa_+ + m)(\kappa_+ - m)\kappa_+}}{m}\exp(\kappa_+ t)\sinh(mt). \quad (17)$$

Solving Eq. (16) using the temporal input mode function $u_{\text{in}}(t)$ that is given in Eq. (17), the stored mode operator is

$$b(0) = \frac{\sqrt{2\gamma_{\text{ext}}}g a_0}{2\sqrt{(\kappa_+ + m)(\kappa_+ - m)\kappa_+}} + \text{noise}. \quad (18)$$

For the case where there are no internal cavity losses and in the limit where the cavity decay rate is much larger than the mechanical dissipation rate $\gamma_o \gg \gamma_m$, it is straightforward to show that the stored mode operator will always be the external operator a_0, in addition to a noise term that includes all possible noises:

$$b(0) = a_0 + \text{noise}. \quad (19)$$

Note that the optimal mode function is obtained from the solutions of Eq. (14) and the mode function is optimal for any arbitrary coupling strength g. In reality, the validity of the linearized interaction Hamiltonian in Eq. (13) might not hold in certain regimes where nonlinear effects cannot be neglected. For those cases, the mode function in Eq. (17) will not be the optimal one. Depending on the observables one wishes to compute, other methods, such as functional optimization, can be used to obtain the optimal mode function.

On the other hand, the transfer field only affects the steady state of the cavity mode in the linearization analyses. In nonlinear simulations, these intense transfer fields give rise to transient behavior in the cavity mode amplitude when transfer fields are switched on or off. They appear as huge spikes in the cavity mode amplitude. Spectral analysis reveals that the frequency contents of the transfer and preparation fields overlap. Moreover, the finite transfer field switching time has significant effects on the efficiency of the optomechanical state transfer. This phenomenon cannot be easily studied in the linearization scheme.

Next, we discuss the issue of the optomechanical state transfer protocol duration. The duration of the writing stage is determined by the temporal input mode function, which we analyze in the following. The input mode function has the form $[e^{(\kappa_+ + m)t} - e^{(\kappa_+ - m)t}]\Theta(-t)$ as in Eq. (17). In the limit where $\gamma_m \ll g \ll \gamma_o$, it can be shown that $\kappa_+ + m \approx \gamma_o, \kappa_+ - m \approx g^2/\gamma_o$ and hence $e^{(\kappa_+ - m)t}\Theta(-t)$ is the dominating term in the temporal input mode function during the writing stage. The duration of the writing stage has to be longer than $1/(\kappa_+ - m)$. In the weak-coupling limit $(g < \gamma_o)$, the pulse duration depends on the ratio between g and γ_o and weaker coupling strength g requires a longer writing stage.

In the strong-coupling limit $(g > \gamma_o)$, m is a complex number and the duration of the writing stage has to be longer than $1/\kappa_+$. The storage time in the mechanical mode is determined by the mechanical dissipation rate and it has to be shorter than $1/\gamma_m$. In this paper, the storage time is restricted to be much smaller than the mechanical lifetime in order to reduce the number of time steps in our simulations. In the state transfer protocol treated here, the output mode is a time-reversed version (around $t = t_s/2$) of the input field, where t_s is storage time of the quantum state in the mechanical mode. Hence, the readout stage duration is chosen as the same as the writing stage. Other protocols are available where the output mode is a symmetric function [37], and in such cases the input and output modes are identical, which is more useful for cascaded quantum logic operations.

Output fields

The output field from the cavity a_{out} contains the signal stored in a single mode, as well as other noises, in all other independent modes. The output field obeys standard input-output theory [30,38–40], which relates the output field to the input and cavity fields. In order to detect and extract the signal, the local oscillator mode in the homodyne detection scheme has to be temporally mode matched to the mode function of the signal. The schematic of the above-mentioned approach is shown in Fig. 3. This extraction is possible due to the orthogonality of these mode functions. Also, due
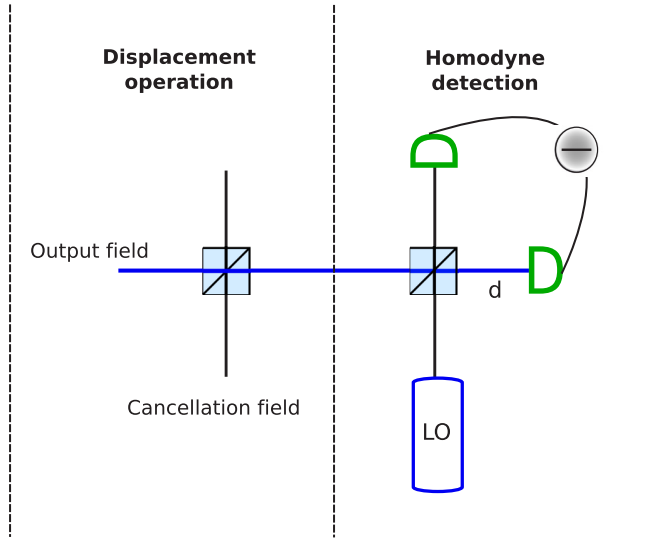
FIG. 3. The transfer field contribution to the output field is subtracted using the cancellation field. The resulting field is then detected with a homodyne detection scheme.

to the time-reversal symmetry of the state transfer protocol around $t = t_s/2$, the output temporal mode function $u_{out}(t)$ is related to the input temporal mode function $u_{in}(t)$ by $u_{out}(t) = u_{in}^*(t_s - t)$, so that

$$u_{out}(t) = 2\frac{\sqrt{(\kappa_+ + m)(\kappa_+ - m)\kappa_+}}{m}\exp[-\kappa_+(t - t_s)]$$
$$\times \sinh[m(T - t)]. \tag{20}$$

The integrated output is obtained using

$$A_{out} = \int_{t_s}^{\infty} u_{out}^*(t)a_{out}(t)\, dt. \tag{21}$$

The integrated output in the linearized approximation is calculated to be

$$A_{out} = \frac{\gamma_{ext}}{2(\kappa_+ + m)(\kappa_+ - m)\kappa_+}$$
$$\times \left(g^2 e^{-\gamma_m t_s} - \gamma_m^2 e^{-\gamma_o t_s}\right)A_{in} + \text{noise}, \tag{22}$$

where $A_{in} = \int_{-\infty}^{0} u_{in}^*(t)a_{in}(t)dt$ is the integrated input.

The advantage of the output mode matching approach for quantum state retrieval is that both the amplitude and phase information of the quantum state are retained. This is crucial for any claim of a working quantum memory.

It is more common, however, to record the output power spectrum in experiments. This is mainly because output power spectra allow the characterization of optomechanical parameters. In the case of optomechanical state transfer, integrating the power spectrum around the signal frequency gives the intensity or energy of the state stored. This can then be compared with the intensity or energy of the input state. The state transfer efficiency is subsequently deduced from the ratio of these two quantities. This method has the drawback of lost information on the phase of the state stored. The quantum nature of the stored state cannot be verified and the claim of a memory device is at best a classical one.

In addition, we observed theoretically that there is overlap in the spectral content between the transfer field and the quantum signal that is retrieved, and this was also observed in recent experiments [20]. This occurs even in the case where the frequency separation between the preparation and transfer field is many orders of magnitude apart, relative to the signal bandwidth.

This observation leads to further complications in the optomechanical state transfer protocol where, for example, filtering of the transfer field spectral content is necessary. Extra processing of the state is not ideal for a quantum memory as the state is not ready to be used for further manipulations, which is essential in quantum information and computational tasks. Nevertheless, the study of optomechanical output spectra is useful in understanding how different optomechanical coupling strengths affect the corresponding cavity responses.

In this paper, we consider the procedure of removing the transfer field amplitude in the output field with a cancellation field. This has also been suggested by Akram *et al.* [41] by mixing the output field with a local oscillator field using a beam splitter. This procedure, achieved in quantum optics experiments [42–44], is nothing but a displacement of the phase-space cavity amplitude by the amplitude due to the transfer field. The Gedanken experiment that corresponds to this method is shown in Fig. 3. An output field containing amplitudes from both the signal α and transfer field β is mixed with a cancellation field A_{cancel} in a beam splitter with transmissivity η. The output port d in Fig. 3, obtained using the standard beam splitter operation, is given by

$$d = \sqrt{\eta}(\alpha + \beta) - \sqrt{1 - \eta}A_{cancel}$$
$$= \sqrt{\eta}\alpha + (\sqrt{\eta}\beta - \sqrt{1 - \eta}A_{cancel}). \tag{23}$$

By setting the transmissivity η close to 1, the amplitude of the cancellation field A_{cancel} is adjusted accordingly to cancel out the second term. It is straightforward to see that a cancellation field A_{cancel} that is much more intense than the transfer field is necessary. Ideally, the cancellation field is split off from the transfer field. This implies that the initial transfer field has to be greatly amplified, which is not always possible. For instance, in order to place the optomechanical system in the strong-coupling regime, a very intense transfer field is needed to enhance the optomechanical coupling. This renders an even more intense cancellation field impractical. This scheme also leads to losses in the signal α, but we treat this rather simple protocol to allow a clear explanation of the issues involved. Other schemes, like a balanced cancellation where the transfer fields are subtracted while the signals are added, may be feasible also.

The phase-space amplitude displacement described above is implemented numerically by simulating the whole state transfer protocol without the preparation field. The mean output field from this simulation is then subtracted from the output field of a full, nonlinear optomechanical state transfer simulation.

V. NUMERICAL SIMULATION

Using the phase-space methods described in Sec. III, it is possible to carry out the corresponding phase-space

simulations using either normally ordered positive P methods or symmetrically ordered truncated Wigner methods that include a truncation approximation. While the first are more precise, the second can be faster, depending on the random sampling error that is required. We carry out both types of calculation, and find that they give results that are the same within sampling error, for these parameter values. We present and discuss the results of our nonlinear phase-space simulations.

A. Electromechanical experiment and parameters

We simulated the quantum memory protocol using electromechanical experiment parameters of Palomaki *et al.* [12]. The experiment demonstrated coherent-state transfer using an electromechanical system, consisting of an LC resonator where one of the plates of the capacitor is movable, behaving like a mechanical oscillator. The resonance frequency of the resonator is $\omega_c/2\pi \approx 7.5$ GHz and the resonance frequency of the mechanical oscillator is $\omega_m/2\pi = 10.5$ MHz. The decay and dissipation rates for the resonator and mechanical oscillator are characterized by $\gamma_o = \gamma_{\text{int}} + \gamma_{\text{ext}}$ and γ_m, respectively. The total decay rate of the resonator, $\gamma_o/2\pi$, is 170 kHz with $\gamma_{\text{ext}}/2\pi = 137.5$ kHz.

The mechanical dissipation rate γ_m is $2\pi \times 17.5$ Hz. The interaction between the resonator and mechanical modes is analogous to the interaction in cavity optomechanics due to the radiation pressure. The coupling between the resonator and mechanical mode is g_0, which is $2\pi \times 200$ Hz in the experiment. The enhanced coupling strength g is defined to be $g_0\sqrt{N}$, where N is the average number of photons in the cavity. The electromechanical system is maintained at 25 μK, which corresponds to an average thermal phonon number of 50. The constant transfer field amplitude ϵ_{trans} is determined from the steady-state solutions of the corresponding stochastic differential equations. It is given by

$$\epsilon_{\text{trans}} = \sqrt{\frac{(\omega_m^2 + \gamma_o^2)N}{2\gamma_{\text{ext}}}}, \qquad (24)$$

where N is the average number of photons in the cavity. The coherent state sent into the electromechanical system has a photon number expectation value of 35 and the storage time in the mechanical oscillator is $t_s = 25$ μs.

We assume both the resonator and mechanical oscillator to be in their ground states initially. This is a good approximation for a resonator in the gigahertz range as the average thermal occupation number is essentially zero at the temperature of order μK, as in the experiment. The mechanical ground state is harder to achieve as it is more susceptible to thermal noise. Besides, theoretical analyses [45,46] showed that, even in the resolved sideband limit ($\omega_m \gg \gamma_o$), there is a nonzero lower bound to the mean mechanical phonon number. However, a mechanical ground state has been achieved in many different experimental implementations of optomechanics. In particular, recent experimental work demonstrated sideband cooling beyond the quantum back-action limit using squeezed light [7]. This allows mechanical quantum ground states to be reached.

B. Numerical methods

All numerical simulations are carried out using xSPDE, which is an open source software package written in MATLAB to solve stochastic differential equations [47]. The numerical results were obtained using a fourth-order Runge-Kutta method in the interaction picture [26,47], with 10^5 parallel trajectories for both the truncated Wigner and positive P simulations.

We express all stochastic differential equations in dimensionless form, by introducing a dimensionless time variable $\tau = \gamma_o t$, where all parameters are relative to the cavity amplitude decay rate, γ_o. This makes clear the regimes of interest. For instance, $\Omega_m = \omega_m/\gamma_o$ determines whether the system is in the resolved sideband regime, which is important for mechanical ground-state cooling [4–6]. The ratio $G = g/\gamma_o$, on the other hand, determines whether the system is in the strong-coupling regime [12,48]. All dimensionless parameters are denoted by capital Greek letters of their corresponding parameters given in Sec. V A, unless stated otherwise.

For instantaneous switching, as used in all the subsections below except Secs. V E and V F, the plots are obtained by first solving the dimensionless stochastic differential equations given in Eq. (4) with a time-dependent input field $E(\tau)$ as follows:

$$E(\tau) = \begin{cases} E_{\text{trans}} + E_{\text{prep}}(\tau), & -\tau_w \leqslant \tau \leqslant 0 \\ 0, & 0 \leqslant \tau \leqslant \tau_s \\ E_{\text{trans}}, & \tau_s \leqslant \tau \leqslant \tau_r \end{cases}, \qquad (25)$$

where τ_w, τ_s, and $\tau_r = \tau_w$ are the durations of the writing, storing, and readout stages, respectively.

The transfer field amplitude $E_{\text{trans}} = \sqrt{(\Omega_m^2 + \Gamma_o^2)N/(2\Gamma_{\text{ext}})}$, and the preparation field amplitude $E_{\text{prep}}(\tau) = \alpha_0 u_{\text{in}}(\tau)$, with coherent-state amplitude $\alpha_0 = \sqrt{N_c}$, where N_c is the coherent photon number that is input for storage. The temporal input mode function is calculated as the optimal one, namely,

$$u_{\text{in}}(\tau) = -2i \frac{\sqrt{(K_+ + M)(K_+ - M)\kappa_+}}{M} e^{(K_+\tau)}$$
$$\times \sinh(M\tau)e^{-i\Omega_m\tau}. \qquad (26)$$

Here, $K_+ = (\Gamma_o + \Gamma_m)/2, \kappa_- = (\Gamma_o - \Gamma_m)/2$ and $M = \sqrt{K_-^2 - G^2}$. In most of the simulations, $N_c = 35$, as in recent coherent-state transfer experiments; however, the effect of storing different input photon numbers on the measurable fidelity is explored in Sec. V F. It should be noted that recent experiments did not use this optimal pulse shape.

In Sec. V E, dealing with finite switching time, a different state transfer protocol is explored in which the transfer fields are turned on and off continuously over a finite time duration. This reduces the spectral width of the transfer field. It is closer to what is actually used in an experiment, although experimental transfer fields may have spectra that differ in detail from the relatively simple models used here. Details of this are given later.

The number of time steps differs for different coupling strengths G, since the optomechanical state transfer protocol duration varies with G. The step in dimensionless time $d\tau$ was chosen to be $1/\{10[\Omega_m + \text{Im}(M)]\}$, where $M = \sqrt{K_-^2 - G^2}$ is defined above. This choice of step in dimensionless time $d\tau$ is much smaller than that stated in the sufficient sampling rate

criterion in the Shannon sampling theorem [49]. Consequently, the finite time-step error, which was calculated by repeating calculations with a step size reduced by 50%, was much less than the relative sampling error, which was typically at most 0.1%.

C. Power spectral densities

The output power spectral density is given by the expectation value:

$$S(\Omega) = \frac{2\pi}{T} \langle \hat{a}_{\text{out}}^{\dagger}(\Omega)\hat{a}_{\text{out}}(\Omega) \rangle, \tag{27}$$

which gives the average dimensionless intensity of the output signal at the dimensionless frequency Ω, over a dimensionless observation time $T = \tau_r - \tau_s$. The frequency domain mode operator $\hat{a}_{\text{out}}(\Omega)$ is defined as the windowed Fourier transform of the time domain mode operator $\hat{a}_{\text{out}}(\tau)$, i.e.,

$$\hat{a}_{\text{out}}(\Omega) = \frac{1}{\sqrt{2\pi}} \int_{\tau_S}^{\tau_r} e^{i\Omega\tau} \hat{a}_{\text{out}}(\tau) \, d\tau, \tag{28}$$

and the operator $\hat{a}^{\dagger}(\Omega)$ is the Hermitian conjugate of the operator $\hat{a}(\Omega)$:

$$\hat{a}_{\text{out}}^{\dagger}(\Omega) = \frac{1}{\sqrt{2\pi}} \int_{0}^{T} e^{-i\Omega\tau} \hat{a}_{\text{out}}^{\dagger}(\tau) \, d\tau. \tag{29}$$

The dimensionless output power spectral density is obtained in the truncated Wigner representation using the relation

$$S(\Omega) = \langle |\alpha_{\text{out}}(\Omega)|^2 \rangle_{\text{Wigner}} - \frac{1}{2}, \tag{30}$$

where $\alpha_{\text{out}}(\Omega)$ is the Fourier transform of the output field amplitude in the truncated Wigner representation $\alpha_{\text{out}}(\tau)$.

From nonlinear numerical simulations, without displacement operations as described in Sec. II B, we observed that the signal and carrier overlap in output spectra. This means that filtering is required for signal extraction. We note that this overlap occurs even when the transfer field and preparation field frequencies are about $2\pi \times 10^7$ Hz apart. This overlap is due to the intense transfer field that drives the electromechanical system.

Figures 4 and 5 show the full, nonlinear output field spectra for $G = 0.5$ and 2.0, respectively, in the truncated Wigner representation. The output field power spectral densities expressed in Eq. (30) are then computed.

We see in Figs. 4 and 5 that the signal content is situated on top of a large amplitude due to the intense transfer field. Even for $G < 1$, the output spectrum is radically different to what is expected for a Lorentzian signal, owing to strong interference between the spectral tails of the transfer field and the signal itself, which has a very low amplitude by comparison. For $G > 1$, the output field spectra exhibit a double-peak feature known as the optomechanical normal mode splitting. First observed experimentally by Gröblacher *et al.* [50] and subsequently with larger G by Teufel *et al.* [51], the optomechanical normal mode splitting with the splitting set by $2G$ is a signature of the strong-coupling regime. Note that the two peaks observed in the output field spectrum are distinctively different from the input spectrum expected for a coherent input, which has a Lorentzian signal. Hence, we expect the fidelity of
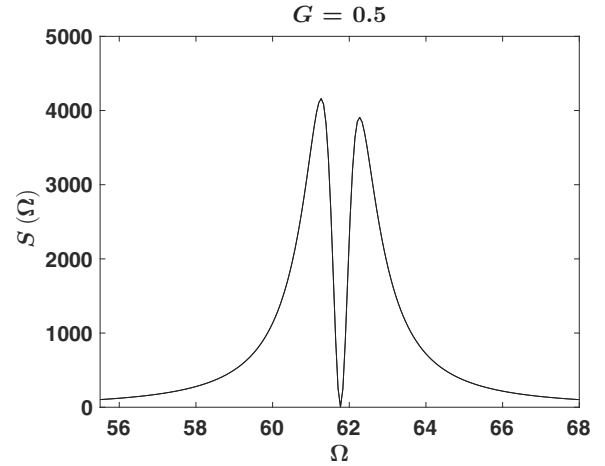

FIG. 4. The output field power spectral density $S(\Omega)$ given in Eq. (30) for $G = 0.5$ from the nonlinear truncated Wigner simulations. The signal is on top of the transfer field frequency content.

the output field with respect to the input field to be lower in the strong-coupling regime than in the weak-coupling regime.

There are a number of ways one can attempt to remove the transfer field contribution in the output field that one detects. In the experimental work by Andrews *et al.* [20], the frequency content of the transfer field around the signal frequency is notch filtered before sending it into the electromechanical system. Another method, as described in Sec. II B, removes the amplitude due to the transfer field in the time domain, using a beam splitter in what is essentially a type of Mach-Zehnder interferometer. Here we adopt the second approach in our nonlinear simulations.

Figures 6(a) and 7(a) show the numerical results for the output field spectra after the displacement operation in the
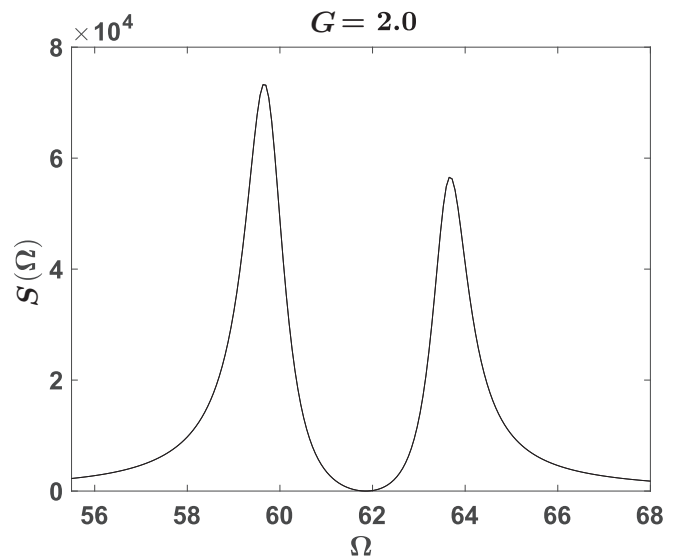

FIG. 5. The output field power spectral density $S(\Omega)$ given in Eq. (30) for $G = 2.0$ from the nonlinear truncated Wigner simulations. The signal is on top of the transfer field frequency content.
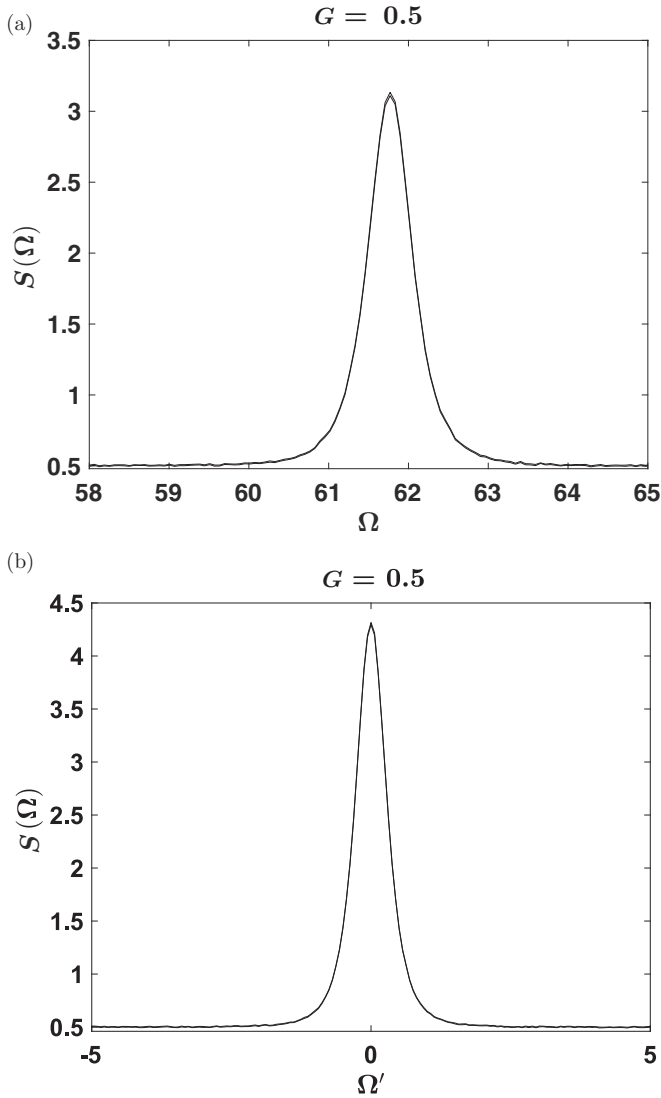
(a)

(b)

FIG. 6. The top figure corresponds to the displaced, output field spectrum in a full, nonlinear truncated Wigner simulation while the bottom figure shows the output field spectrum of a linearized truncated Wigner simulation. The dimensionless signal frequency in the nonlinear simulation is at $\Omega = \Omega_m$ as the system is in the rotating frame of the transfer field, while the dimensionless signal frequency in the linearized simulation is at $\Omega' = 0$. The number of samples taken is 10^5.
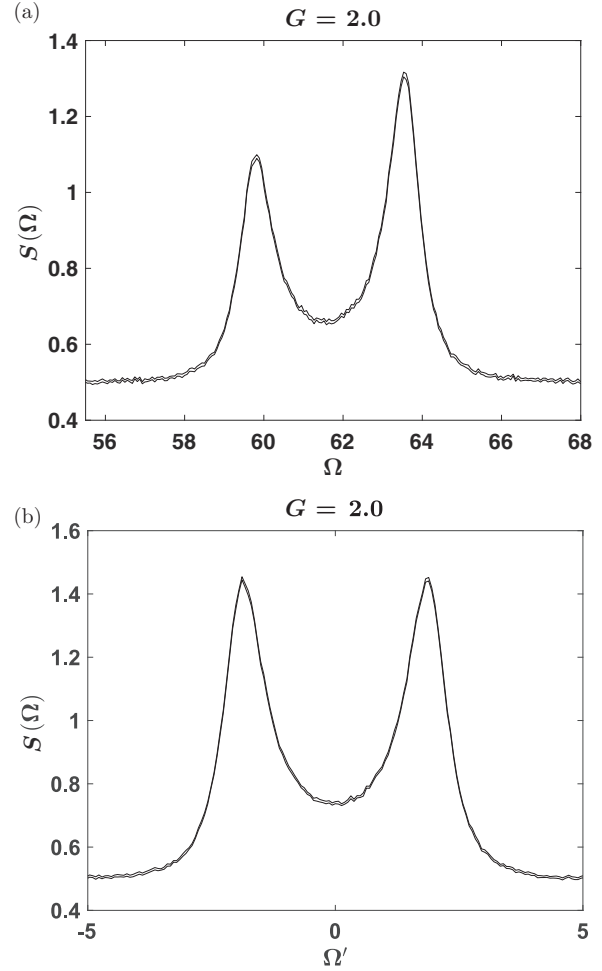
(a)

(b)

FIG. 7. The top figure corresponds to the displaced output field spectrum in a full, nonlinear truncated Wigner simulation while the bottom figure shows the output field spectrum of a linearized truncated Wigner simulation. Axes labels are as for Fig. 6. The number of samples taken is 10^5.

nonlinear truncated Wigner simulations. Also plotted are the output field spectra obtained from the linearized truncated Wigner simulations as shown in Figs. 6(b) and 7(b). These plots are obtained by solving stochastic differential equations as given in Eq. (14), in the dimensionless form with the

TABLE I. The efficiency of the state transfer protocol as defined in Eq. (34), for different coupling strengths G with instantaneous transfer field switching. These values are obtained from positive P simulations.

G	Integrated input, A_{in}	Integrated output, A_{out}	$\zeta_{\text{instant}} \equiv \dfrac{|A_{\text{out}}|}{|A_{\text{in}}|}$
0.50	5.9161	$(4.7716 + 0.0971i) \pm (0.0056 + 0.0063i)$	0.8067 ± 0.0010
0.75	5.9161	$(4.7697 + 0.1869i) \pm (0.0052 + 0.0056i)$	0.8068 ± 0.0009
1.00	5.9161	$(4.7604 + 0.2890i) \pm (0.0062 + 0.0071i)$	0.8061 ± 0.0012
1.25	5.9161	$(4.7458 + 0.4328i) \pm (0.0067 + 0.0075i)$	0.8055 ± 0.0011
1.50	5.9161	$(4.7176 + 0.6097i) \pm (0.0054 + 0.0062i)$	0.8041 ± 0.0010
1.75	5.9161	$(4.6612 + 0.8108i) \pm (0.0095 + 0.0057i)$	0.7997 ± 0.0017
2.00	5.9161	$(4.5943 + 1.0495i) \pm (0.0089 + 0.0119i)$	0.7966 ± 0.0016

TABLE II. The efficiency of the state transfer protocol as defined in Eq. (34), for different coupling strengths G with instantaneous transfer field switching. These values are obtained from truncated Wigner simulations.

G	Integrated input, A_{in}	Integrated output, A_{out}	$\zeta_{\text{instant}} \equiv \frac{|A_{\text{out}}|}{|A_{\text{in}}|}$
0.50	$(5.9146 - 0.0025i) \pm (0.0023 + 0.0025i)$	$(4.7675 + 0.0939i) \pm (0.0028 + 0.0022i)$	0.8062 ± 0.0002
0.75	$(5.9160 + 0.0010i) \pm (0.0020 + 0.0021i)$	$(4.7651 + 0.1768i) \pm (0.0033 + 0.0026i)$	0.8060 ± 0.0003
1.00	$(5.9169 + 0.0006i) \pm (0.0017 + 0.0024i)$	$(4.7576 + 0.2896i) \pm (0.0028 + 0.0030i)$	0.8056 ± 0.0003
1.25	$(5.9152 + 0.0007i) \pm (0.0026 + 0.0016i)$	$(4.7431 + 0.4349i) \pm (0.0028 + 0.0021i)$	0.8052 ± 0.0002
1.50	$(5.9167 - 0.0008i) \pm (0.0015 + 0.0027i)$	$(4.7119 + 0.6098i) \pm (0.0034 + 0.0034i)$	0.8030 ± 0.0003
1.75	$(5.9167 + 0.0013i) \pm (0.0025 + 0.0018i)$	$(4.6669 + 0.8135i) \pm (0.0040 + 0.0029i)$	0.8007 ± 0.0004
2.00	$(5.9139 + 0.0003i) \pm (0.0021 + 0.0023i)$	$(4.5996 + 1.0445i) \pm (0.0021 + 0.0034i)$	0.7976 ± 0.0002

effective coupling strength

$$G(\tau) = \begin{cases} G, & -\tau_w \leqslant \tau \leqslant 0 \\ 0, & 0 \leqslant \tau \leqslant \tau_s \\ G, & \tau_s \leqslant \tau \leqslant \tau_r \end{cases} \tag{31}$$

and the input field

$$E(\tau) = \begin{cases} E_{\text{prep}}(\tau), & -\tau_w \leqslant \tau \leqslant 0 \\ 0, & \text{otherwise} \end{cases}, \tag{32}$$

where $E_{\text{prep}}(\tau) = \alpha_0 u_{\text{in}}(\tau)$, with the coherent-state amplitude $\alpha_0 = \sqrt{35}$ and the temporal input mode function

$$u_{\text{in}}(\tau) = -2i \frac{\sqrt{(K_+ + M)(K_+ - M)\kappa_+}}{M} e^{(K_+\tau)} \sinh(M\tau). \tag{33}$$

The signal frequency in the linearized simulations is at $\Omega' = 0$ while the signal frequency in the nonlinear simulations is at $\Omega = \Omega_m$ since we transformed into the rotating frame of the transfer field. The large quantitative differences found indicate that even a highly idealized amplitude cancellation protocol is insufficient to recover the linearized spectral predictions, showing that nonlinear effects are important in these experiments.

D. Integrated input and output modes using temporal mode functions

Using the temporal mode functions introduced in Sec. II B, the energy retrieved with respect to the energy stored can be computed straightforwardly. However, due to the fact that the stored cavity amplitude in a particular mode contains a contribution from the transfer field, we remove this amplitude via a displacement operation in the phase space as described in Sec. II B. We integrate the input and output modes with their corresponding temporal mode functions to pick out the desired input and output signals. The efficiency of the protocol is defined to be

$$\zeta_{\text{instant}} \equiv \frac{|A_{\text{out}}|}{|A_{\text{in}}|}. \tag{34}$$

We obtain numerical results for the state transfer energy efficiencies for different coupling strengths using both the truncated Wigner and positive P representations. The numerical results are shown in Tables I and II. They are obtained by solving the dimensionless form of stochastic differential equations given in Eqs. (4) and (9) for the truncated Wigner and positive P representations, respectively, with the

time-dependent input field $E(\tau)$ as described in Eq. (25). The integrated input is

$$A_{\text{in}} = \int_{-\infty}^{0} u_{\text{in}}^*(\tau)\left[E(\tau) + \alpha_{\text{ext}}^{\text{in}}\right] d\tau, \tag{35}$$

where $u_{\text{in}}(\tau)$ is defined in Eq. (26) and $\alpha_{\text{ext}}^{\text{in}}$ is thermal Gaussian noise. The integrated output is given by

$$A_{\text{out}} = \int_{\tau_s}^{\infty} u_{\text{out}}^*(\tau)\alpha_{\text{out}}(\tau) d\tau. \tag{36}$$

Here, the temporal output mode function $u_{\text{out}}(\tau) = u_{\text{in}}^*(\tau_s - \tau)$ and the dimensionless output field $\alpha_{\text{out}}(\tau)$ is obtained from the input-output relation as in Eq. (7).

These numerical results are compared with the analytical result given in Eq. (22) in Fig. 8. The analytical results plotted here give the first term in Eq. (22), ignoring the additional noise term. The errors in the error bars in Fig. 8 include both the sampling error and time-step error. The main source of error is the sampling error.

It can be easily seen from the tables and figures that the two types of numerical simulation generate very similar results up to the numerical sampling error. The Wigner truncation error is negligible for these calculations, even though the coherent signal amplitude is not very large. However, the analytical predictions using linearization give large errors for $G > 1$.
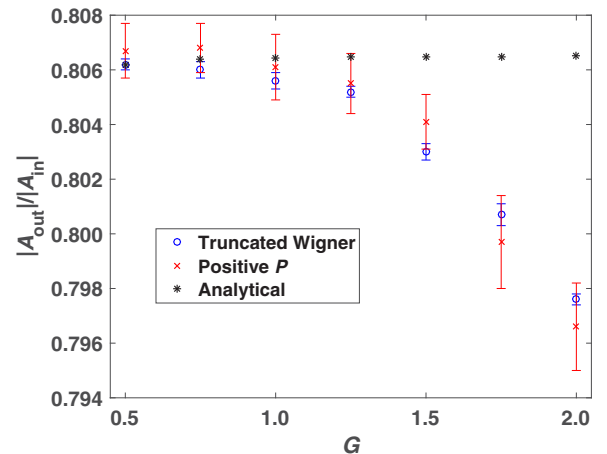

FIG. 8. The efficiency of the state transfer protocol for different coupling strengths G. The number of samples taken for both the truncated Wigner and positive P simulations is 10^5. The error bars denote the sampling errors in our phase-space simulations.

TABLE III. The efficiency of the state transfer protocol as the ratio between the integrated output A_{out} and integrated input A_{in}. These are computed for different coupling strengths G with finite transfer field switching time. These values are obtained from positive P simulations.

G	Integrated input, A_{in}	Integrated output, A_{out}	$\zeta_{\text{finite}} \equiv \frac{|A_{\text{out}}|}{|A_{\text{in}}|}$
0.50	5.9161	$(4.7561 + 0.1106i) \pm (0.0053 + 0.0048i)$	0.8041 ± 0.0008
0.75	5.9161	$(4.7515 + 0.1951i) \pm (0.0068 + 0.0077i)$	0.8038 ± 0.0010
1.00	5.9161	$(4.7124 + 0.2773i) \pm (0.0047 + 0.0041i)$	0.7979 ± 0.0008
1.25	5.9161	$(4.6761 + 0.4056i) \pm (0.0067 + 0.0056i)$	0.7934 ± 0.0010
1.50	5.9161	$(4.6300 + 0.5759i) \pm (0.0058 + 0.0068i)$	0.7886 ± 0.0010
1.75	5.9161	$(4.5441 + 0.7632i) \pm (0.0044 + 0.0074i)$	0.7788 ± 0.0009
2.00	5.9161	$(4.4531 + 0.9661i) \pm (0.0079 + 0.0068i)$	0.7702 ± 0.0013

E. Finite switching time

The state transfer protocol with minimal degradation relies on having the optimal, enhanced coupling strength $G = g_0\sqrt{N}/\gamma_o$, where N is determined by the transfer field amplitude as in Eq. (24). In practice, it takes time to switch the transfer field to its required amplitude. Hence, the efficiency of the state transfer protocol defined in Eq. (34) depends on how fast the transfer field can be turned on and off. Within the linearized approximation, the finite switching time of the transfer field cannot be easily taken into account. A full, nonlinear simulation then becomes both more accurate and simpler to carry out. We run the same numerical simulations as in Sec. V D, except that the transfer field is now time dependent, to take into account the finite switching of the field. In this paper, we model the finite transfer field switching with a smoothing function as follows:

$$E_{\text{trans}}(\tau) = \begin{cases} E_{\text{trans}} \cos^2\left[\frac{(\tau-\tau_1)}{\tau_1+\tau_w}\frac{\pi}{2}\right], & -\tau_w \leqslant \tau \leqslant \tau_1 \\ E_{\text{trans}}, & \tau_1 \leqslant \tau \leqslant \tau_2 \\ E_{\text{trans}} \cos^2\left[\frac{(\tau_2-\tau)}{\tau_2}\frac{\pi}{2}\right], & \tau_2 \leqslant \tau \leqslant 0 \\ 0, & 0 \leqslant \tau \leqslant \tau_s \\ E_{\text{trans}} \cos^2\left[\frac{(\tau_r-\tau)}{\tau_r-\tau_3}\frac{\pi}{2}\right], & \tau_s \leqslant \tau \leqslant \tau_3 \\ E_{\text{trans}}, & \tau_3 \leqslant \tau \leqslant \tau_r \end{cases} \quad (37)$$

Here, $E_{\text{trans}}(\tau)$ is the time-dependent transfer field and its constant amplitude $E_{\text{trans}} = \sqrt{(\Omega_m^2 + \Gamma_o^2)N/(2\Gamma_{\text{ext}})}$. The dimensionless time τ_w is the length of the writing stage, τ_1 is the time when the writing stage transfer field is fully turned on, τ_2 is the time when the writing stage transfer field starts to turn off, τ_3 is the time we start turning on the readout stage transfer field, τ_4 is when the readout stage transfer field is fully turned on, and τ_r is the length of the readout stage. As described in Sec. II B, the duration of the writing stage is the real part of $1/(K_+ - M)$,

where $K_+ = (\Gamma_o + \Gamma_m)/2$, $K_- = (\Gamma_o - \Gamma_m)/2$, $\Gamma_m = \gamma_m/\gamma_o$, and $M = \sqrt{K_-^2 - G^2}$.

We choose the switching time to be 1% of the duration of the writing stage. The resulting efficiencies are shown in Tables III and IV. The reduced efficiency in percentage relative to the efficiency with instantaneous switching is defined as

$$\zeta_{\text{reduced}} = \frac{\zeta_{\text{finite}} - \zeta_{\text{instant}}}{\zeta_{\text{instant}}} \times 100\%, \quad (38)$$

where ζ_{finite} is the efficiency, taking the finite transfer field switching into account. The results are plotted in Fig. 9.

F. Quantum fidelity

In this paper, we compute the quantum fidelity in the truncated Wigner representation. We note that the quantum fidelity computation in the positive P representation is nontrivial as the sampling error can be very large [52]. It was observed by Rosales-Zárate and Drummond [52] that a generalized Gaussian phase-space representation is more suited for computing the quantum fidelity exactly.

The quantum fidelity is defined as

$$F = \text{Tr}(\rho_i \rho_f), \quad (39)$$

where ρ_i is the density operator of the stored quantum state and ρ_f is the density operator of the retrieved quantum state. The quantum fidelity in the truncated Wigner representation is given by [53,54]

$$F = \pi \int W_i(\alpha) W_f(\alpha) \, d^2\alpha. \quad (40)$$

Here, $W_i(\alpha)$ and $W_f(\alpha)$ are the corresponding Wigner functions for ρ_i and ρ_f, respectively. In particular, for a coherent

TABLE IV. The efficiency of the state transfer protocol as the ratio between the integrated output A_{out} and integrated input A_{in}. These are computed for different coupling strengths G with finite transfer field switching time. These values are obtained from truncated Wigner simulations.

| G	Integrated input, A_{in}	Integrated output, A_{out}	$\zeta_{\text{finite}} \equiv \frac{|A_{\text{out}}|}{|A_{\text{in}}|}$
0.50	$(5.9146 - 0.0025i) \pm (0.0023 + 0.0025i)$	$(4.7566 + 0.0957i) \pm (0.0028 + 0.0022i)$	0.8044 ± 0.0002
0.75	$(5.9160 + 0.0010i) \pm (0.0020 + 0.0021i)$	$(4.7409 + 0.1781i) \pm (0.0031 + 0.0026i)$	0.8019 ± 0.0003
1.00	$(5.9169 + 0.0006i) \pm (0.0017 + 0.0024i)$	$(4.7149 + 0.2860i) \pm (0.0028 + 0.0030i)$	0.7983 ± 0.0003
1.25	$(5.9152 + 0.0007i) \pm (0.0026 + 0.0016i)$	$(4.6777 + 0.4226i) \pm (0.0028 + 0.0022i)$	0.7940 ± 0.0002
1.50	$(5.9167 - 0.0008i) \pm (0.0015 + 0.0027i)$	$(4.6205 + 0.5837i) \pm (0.0029 + 0.0034i)$	0.7871 ± 0.0004
1.75	$(5.9167 + 0.0013i) \pm (0.0025 + 0.0018i)$	$(4.5485 + 0.7684i) \pm (0.0039 + 0.0026i)$	0.7797 ± 0.0004
2.00	$(5.9139 + 0.0003i) \pm (0.0021 + 0.0023i)$	$(4.4532 + 0.9747i) \pm (0.0021 + 0.0035i)$	0.7708 ± 0.0002
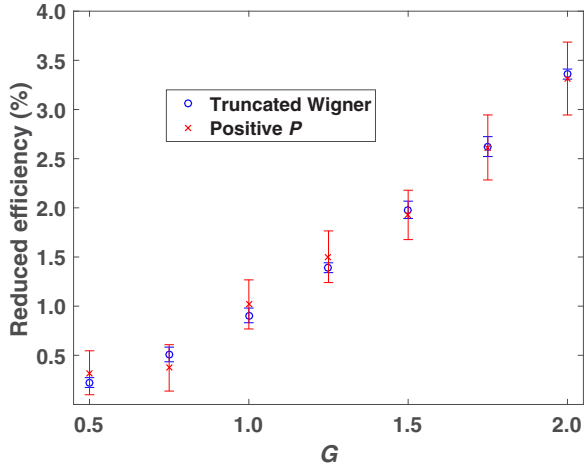
FIG. 9. The reduced efficiency of the state transfer protocol due to finite switching for different coupling strengths G. The number of samples taken for both the truncated Wigner and positive P simulations is 10^5. The error bars denote the sampling errors in our phase-space simulations.

state $|\alpha_0\rangle$, the corresponding Wigner function is given by

$$W(\alpha) = \frac{2}{\pi}\exp(-2|\alpha - \alpha_0|^2). \tag{41}$$

The quantum fidelity can then be computed using a Monte Carlo method as follows:

$$F = \pi \int W_i(\alpha)W_f(\alpha)\,d^2\alpha \approx \frac{\pi}{N_{\text{sample}}} \sum_{j=1}^{N_{\text{sample}}} W_i(\alpha_j)$$

$$= \frac{2}{N_{\text{sample}}} \sum_{j=1}^{N_{\text{sample}}} \exp(-2|\alpha_j - \alpha_0|^2). \tag{42}$$

The fidelity for different coupling strengths is tabulated in Table V, for our canonical example of a 35 photon coherent signal as described in previous sections, including transfer field cancellation. The fidelity, taking into account the effect of finite transfer field switching time, is shown in Table VI. The results show a decrease in fidelity when the transfer field takes a finite time to turn on and off, compared to the case where transfer field is assumed to be switched instantaneously. This is expected since the efficiency of the state transfer protocol as defined in Eq. (34) is reduced in the case of finite transfer field switching time.

TABLE V. The fidelity of the optomechanical state transfer protocol with instantaneous transfer field switching. These values are obtained from truncated Wigner simulations.

G	Fidelity, F
0.50	0.2772 ± 0.0012
0.75	0.2702 ± 0.0015
1.00	0.2553 ± 0.0014
1.25	0.2276 ± 0.0013
1.50	0.1847 ± 0.0016
1.75	0.1325 ± 0.0014
2.00	0.0820 ± 0.0008

TABLE VI. The fidelity of the optomechanical state transfer protocol with finite transfer field switching time as described in Sec. V E. The fidelity is lower compared to the case of instantaneous transfer field switching. These values are obtained from truncated Wigner simulations.

G	Fidelity, F
0.50	0.2716 ± 0.0013
0.75	0.2585 ± 0.0015
1.00	0.2359 ± 0.0012
1.25	0.2028 ± 0.0014
1.50	0.1578 ± 0.0012
1.75	0.1098 ± 0.0014
2.00	0.0665 ± 0.0006

Hammerer *et al.* [22] computed the minimum fidelity F_{min} required for a quantum memory and it is given by

$$F \geqslant \frac{(1 + N_c)}{(2N_c + 1)} \equiv F_{\text{min}}, \tag{43}$$

where N_c is the mean photon number of the quantum state one wishes to store. The criterion in Eq. (43) provides a benchmark for the quantum memory of a coherent state. Assuming that both the input and output states are pure coherent states with amplitudes α_0 and $\eta\alpha_0$, respectively, the quantum fidelity of the coherent output state $|\eta\alpha_0\rangle$ with respect to the coherent input state $|\alpha_0\rangle$ is given by

$$F_{\text{pure}} = |\langle\eta\alpha_0|\alpha_0\rangle|^2 = \exp[-|\alpha_0(1 - \eta)|^2]. \tag{44}$$

Here $\eta = 0.8088$ is the overall amplitude storage efficiency, giving an upper bound on possible fidelity, as quoted in the experiment by Palomaki *et al.* [12].

As suggested by Eqs. (43) and (44), the state transfer protocol fidelity and its minimum value required for a quantum memory of a coherent state depend on the mean photon number of the coherent state. We computed the fidelities F for coherent states with mean photon number 1,5,15,25, and 35, for $G = 0.5$ with instantaneous transfer field switching. They are carried out in the truncated Wigner representation. These fidelities are then compared to F_{min} and F_{pure} predicted by Eqs. (43) and (44), respectively, as shown in Table VII. From the table, we see that F_{pure} is quantitatively different from fidelity F computed numerically. The discrepancies increase with smaller mean photon numbers of the corresponding coherent states. This is because a coherent state with small mean photon number is more susceptible to noise from the environment and hence the assumption that the output state is a pure coherent state is invalid.

On the other hand, the fidelities for coherent states with smaller mean photon numbers are increased to the point that they do exceed F_{min}. For these cases, a genuine quantum optomechanical memory of a coherent state can be achieved. For larger mean photon numbers the fidelity is reduced, since the losses will lead to a substantial probability of an output state with a different photon number, that is therefore orthogonal to the input. In these cases, the predicted fidelity is lower than that required by the criterion in Eq. (43). In order to achieve quantum state transfer, the stored photon numbers of the internal cavity losses and thermal noises on the mechanical

TABLE VII. Fidelities for different number of photons. Here, N_c is the mean photon number of the corresponding coherent state one wishes to store. Fidelities F are obtained from truncated Wigner simulations. These are compared with the corresponding fidelities as given in Eq. (44) and also the minimum fidelities required for claiming a quantum memory for a coherent state, as in Eq. (43).

N_c	F	F_{pure}	F_{min}
1	0.7694 ± 0.0027	0.9641	0.6667
5	0.6825 ± 0.0026	0.8329	0.5455
15	0.5055 ± 0.0019	0.5779	0.5161
25	0.3743 ± 0.0016	0.4009	0.5098
35	0.2772 ± 0.0012	0.2782	0.5070

oscillator have to be significantly reduced compared to a recent experiment on coherent-state transfer.

VI. CONCLUSION

Full, nonlinear simulations of an optomechanical quantum state transfer protocol were carried out, using both the truncated Wigner and positive P representations. We observed nonlinear effects and strong spectral tails due to the presence of the red-detuned transfer field that is used to facilitate the optomechanical state transfer. Further experimental operations are needed to retrieve the states stored in a quantum memory. For experiments with stronger optomechanical coupling strengths, even reaching the strong quantum coupling regime, the nonlinearity of the system cannot be neglected and linearization approximation breaks down. These nonlinear optomechanical systems are best simulated in practice using phase-space methods.

Most experiments to date infer state transfer efficiency from the energy retrieved from a state transfer protocol. To achieve a quantum memory, both the amplitude and phase information of a quantum state have to be stored and retrieved. A more suitable measure is the fidelity. The fidelity is computed numerically here using realistic experimental parameters. The results are lower than that required for true quantum state transfers for large photon numbers. We show that either the use of coherent inputs with smaller photon numbers or improvements in the quality factor of the cavity and mechanical systems will, however, increase the fidelity beyond the threshold required for a quantum memory.

[1] J. I. Cirac, P. Zoller, H. J. Kimble, and H. Mabuchi, Phys. Rev. Lett. **78**, 3221 (1997).

[2] H. J. Kimble, Nature (London) **453**, 1023 (2008).

[3] S. Ritter, C. Nölleke, C. Hahn, A. Reiserer, A. Neuzner, M. Uphoff, M. Mücke, E. Figueroa, J. Bochmann, and G. Rempe, Nature (London) **484**, 195 (2012).

[4] A. Schliesser, R. Rivière, G. Anetsberger, O. Arcizet, and T. J. Kippenberg, Nature Physics **4**, 415 (2008).

[5] J. Teufel, T. Donner, D. Li, J. Harlow, M. Allman, K. Cicak, A. Sirois, J. D. Whittaker, K. Lehnert, and R. W. Simmonds, Nature (London) **475**, 359 (2011).

[6] J. Chan, T. M. Alegre, A. H. Safavi-Naeini, J. T. Hill, A. Krause, S. Gröblacher, M. Aspelmeyer, and O. Painter, Nature (London) **478**, 89 (2011).

[7] J. B. Clark, F. Lecocq, R. W. Simmonds, J. Aumentado, and J. D. Teufel, Nature (London) **541**, 191 (2017).

[8] S. G. Hofer, W. Wieczorek, M. Aspelmeyer, and K. Hammerer, Phys. Rev. A **84**, 052327 (2011).

[9] S. Mancini, V. Giovannetti, D. Vitali, and P. Tombesi, Phys. Rev. Lett. **88**, 120401 (2002).

[10] V. Giovannetti, S. Mancini, and P. Tombesi, Europhys. Lett. **54**, 559 (2001).

[11] J. Zhang, K. Peng, and S. L. Braunstein, Phys. Rev. A **68**, 013808 (2003).

[12] T. Palomaki, J. Harlow, J. Teufel, R. Simmonds, and K. Lehnert, Nature (London) **495**, 210 (2013).

[13] T. A. Palomaki, J. D. Teufel, R. W. Simmonds, and K. W. Lehnert, Science **342**, 710 (2013).

[14] Q. Y. He and M. D. Reid, Phys. Rev. A **88**, 052121 (2013).

[15] S. Kiesewetter, Q. Y. He, P. D. Drummond, and M. D. Reid, Phys. Rev. A **90**, 043805 (2014).

[16] M. Aspelmeyer, T. J. Kippenberg, and F. Marquardt, Rev. Mod. Phys. **86**, 1391 (2014).

[17] E. Wigner, Phys. Rev. **40**, 749 (1932).

[18] R. Graham and F. Haake, *Quantum Statistics in Optics and Solid-State Physics*, Ergebnisse der exakten Naturwissenschaften (Springer, New York, 1973).

[19] P. D. Drummond and C. W. Gardiner, J. Phys. A **13**, 2353 (1980).

[20] R. W. Andrews, A. P. Reed, K. Cicak, J. D. Teufel, and K. W. Lehnert, Nat. Commun. **6**, 10021 (2015).

[21] Q. Y. He, M. D. Reid, E. Giacobino, J. Cviklinski, and P. D. Drummond, Phys. Rev. A **79**, 022310 (2009).

[22] K. Hammerer, M. M. Wolf, E. S. Polzik, and J. I. Cirac, Phys. Rev. Lett. **94**, 150503 (2005).

[23] H. Carmichael, *Statistical Methods in Quantum Optics 1: Master Equations and Fokker-Planck Equations*, Theoretical and Mathematical Physics (Springer, Berlin, 2013).

[24] P. Meystre, Ann. Phys. **525**, 215 (2013).

[25] J.-Q. Liao, H. K. Cheung, and C. K. Law, Phys. Rev. A **85**, 025803 (2012).

[26] P. Drummond and I. Mortimer, J. Comput. Phys. **93**, 144 (1991).

[27] P. Kloeden and E. Platen, *Numerical Solution of Stochastic Differential Equations*, Stochastic Modelling and Applied Probability (Springer, Berlin, 2011).

[28] D. J. Higham, SIAM Rev. **43**, 525 (2001).

[29] C. Gardiner, *Handbook of Stochastic Methods for Physics, Chemistry, and the Natural Sciences*, Springer Complexity (Springer, New York, 2004).

[30] C. W. Gardiner and M. J. Collett, Phys. Rev. A **31**, 3761 (1985).

[31] P. D. Drummond and P. Kinsler, Phys. Rev. A **40**, 4813 (1989).

[32] P. D. Drummond, K. Dechoum, and S. Chaturvedi, Phys. Rev. A **65**, 033806 (2002).

[33] P. Kinsler, Phys. Rev. A **53**, 2000 (1996).

[34] A. Gilchrist, C. W. Gardiner, and P. D. Drummond, Phys. Rev. A **55**, 3014 (1997).

[35] P. Deuar and P. D. Drummond, Phys. Rev. A **66**, 033812 (2002).

[36] S. Kiesewetter, R. Y. Teh, P. D. Drummond, and M. D. Reid, Phys. Rev. Lett. **119**, 023601 (2017).

[37] Q. Y. He, M. D. Reid, and P. D. Drummond, Opt. Express **17**, 9662 (2009).

[38] B. Yurke and J. S. Denker, Phys. Rev. A **29**, 1419 (1984).

[39] M. J. Collett and C. W. Gardiner, Phys. Rev. A **30**, 1386 (1984).

[40] B. Yurke, Phys. Rev. A **32**, 300 (1985).

[41] U. Akram, N. Kiesel, M. Aspelmeyer, and G. J. Milburn, New J. Phys. **12**, 083030 (2010).

[42] A. Furusawa, J. L. Sørensen, S. L. Braunstein, C. A. Fuchs, H. J. Kimble, and E. S. Polzik, Science **282**, 706 (1998).

[43] W. P. Bowen, N. Treps, B. C. Buchler, R. Schnabel, T. C. Ralph, Hans-A. Bachor, T. Symul, and P. K. Lam, Phys. Rev. A **67**, 032302 (2003).

[44] C. Wittmann, U. L. Andersen, M. Takeoka, D. Sych, and G. Leuchs, Phys. Rev. Lett. **104**, 100505 (2010).

[45] F. Marquardt, J. P. Chen, A. A. Clerk, and S. M. Girvin, Phys. Rev. Lett. **99**, 093902 (2007).

[46] I. Wilson-Rae, N. Nooshi, W. Zwerger, and T. J. Kippenberg, Phys. Rev. Lett. **99**, 093901 (2007).

[47] S. Kiesewetter, R. Polkinghorne, B. Opanchuk, and P. D. Drummond, SoftwareX **5**, 12 (2016).

[48] E. Verhagen, S. Deléglise, S. Weis, A. Schliesser, and T. J. Kippenberg, Nature (London) **482**, 63 (2012).

[49] C. E. Shannon, Proc. IRE **37**, 10 (1949).

[50] S. Gröblacher, K. Hammerer, M. R. Vanner, and M. Aspelmeyer, Nature (London) **460**, 724 (2009).

[51] J. D. Teufel, D. Li, M. S. Allman, K. Cicak, A. J. Sirois, J. D. Whittaker, and R. W. Simmonds, Nature (London) **471**, 204 (2011).

[52] L. E. C. Rosales-Zárate and P. D. Drummond, Phys. Rev. A **84**, 042114 (2011).

[53] K. E. Cahill and R. J. Glauber, Phys. Rev. **177**, 1882 (1969).

[54] B. Schumacher, Phys. Rev. A **54**, 2614 (1996).